Structure Parameters of Synaptic Vesicles Quantified by Small-Angle X-Ray Scattering

Simon Castorph,[†*] Dietmar Riedel,[‡] Lise Arleth,[§] Michael Sztucki,[¶] Reinhard Jahn,[‡] Matthew Holt,[‡*] and Tim Salditt[†*]

[†]Institut für Röntgenphysik, Universität Göttingen, Göttingen, Germany; [‡]Max Planck Institut für Biophysikalische Chemie, Department of Neurobiology, Göttingen, Germany; [§]Biophysics, Faculty of Life Sciences, University of Copenhagen, Frederiksberg, Denmark; and [¶]European Synchrotron Radiation Facility, Grenoble, France

ABSTRACT Synaptic vesicles (SVs) are small, membrane-bound organelles that are found in the synaptic terminal of neurons, and which are crucial in neurotransmission. After a rise in internal [Ca^{2+}] during neuronal stimulation, SVs fuse with the plasma membrane releasing their neurotransmitter content, which then signals neighboring neurons. SVs are subsequently recycled and refilled with neurotransmitter for further rounds of release. Recently, tremendous progress has been made in elucidating the molecular composition of SVs, as well as putative protein-protein interactions. However, what is lacking is an empirical description of SV structure at the supramolecular level—which is necessary to enable us to fully understand the processes of membrane fusion, retrieval, and recycling. Using small-angle x-ray scattering, we have directly investigated the size and structure of purified SVs. From this information, we deduced detailed size and density parameters for the protein layers responsible for SV function, as well as information about the lipid bilayer. To achieve a convincing model fit, a laterally anisotropic structure for the protein shell is needed, as a rotationally symmetric density profile does not explain the data. Not only does our model confirm many of the preexisting ideas concerning SV structure, but also for the first time, to our knowledge, it indicates structural refinements, such as the presence of protein microdomains.

INTRODUCTION

Synaptic vesicles (SVs) are secretory organelles that store neurotransmitter in presynaptic nerve endings. When an action potential arrives in the nerve terminal, the plasma membrane is depolarized, leading to the opening of voltage-gated [Ca^{2+}] channels in the plasma membrane. The accompanying rise in intracellular [Ca^{2+}] leads to the fusion (exocytosis) of the synaptic vesicles with the plasma membrane, resulting in the release of neurotransmitter. After exocytosis, SV membrane is recovered by endocytosis and used to reform vesicles, which are then refilled with neurotransmitter and used for a subsequent round of exocytosis (1). As the synaptic vesicle is the only constant during this cycle, it must be able to coordinate the process.

Fortunately, the analysis of SVs is simplified by the fact that they can be purified to apparent homogeneity in large quantities, making them amenable to biochemical studies. This purification is possible because they are very abundant in brain tissue (~5% of the protein in the central nervous system) and smaller and more homogeneous in size and shape than most other organelles, allowing the application of mild size fractionation techniques.

In a primary approach to understanding SV function, individual proteins on isolated vesicles were identified and their functions elucidated, such as synaptobrevin, which is the SNARE protein thought to play a role in exocytosis (2). A preliminary analysis of lipid composition was also performed (3). Work from several laboratories over the years culminated in the recent publication of a molecular model that attempted to integrate all quantitative data on the protein and lipid composition of the vesicle (4).

Despite these efforts, what is still lacking is an empirical description of SV structure at the supramolecular level, which is necessary to fully describe the processes of membrane fusion, retrieval, and recycling for our understanding. Importantly, such an assessment of SV structure, compatible with more physiological conditions and with higher (near molecular) resolution, can be effectively cross-validated by these recent, independent studies. Unfortunately, the property that allows vesicle purification (small size) complicates structural analysis. For instance, advanced light microscopy techniques (e.g., photoactivated localization microscopy) are at the limit of the spatial resolution required. In contrast, electron microscopy techniques, such as cryo-electron microscopy and quick-freeze deep-etch microscopy, can provide detailed structural information on the conformation of protein (complexes), but both fail to provide detailed structural information about the lipid environment of the protein (complex) under investigation. Further, care has to be taken, as these methods are prone to method-specific artifacts. Small-angle x-ray scattering (SAXS), on the other hand, is a well-established technique that has traditionally been used for the ensemble solution structure of biomolecules (5), or larger, regular-shaped structures, such as virus capsids (6). Importantly, the technique is also capable of providing detailed information about lipid structures and associated proteins, under quasiphysiological conditions.

Submitted August 27, 2009, and accepted for publication December 1, 2009.

*Correspondence: scastor@gwdg.de, mholt@gwdg.de, or tsaldit@gwdg.de

Editor: Huey W. Huang.

0006-3495/10/04/1200/9 $2.00

doi: 10.1016/j.bpj.2009.12.4278

Here we demonstrate that SAXS is an ideal technique to study the (heterogeneous) supramolecular structure of a functional organelle on an absolute scale.

We derive the average radial density profile $\rho(r)$, as well as the polydispersity function $p(R)$, on an absolute scale, with no free prefactors. Importantly, our measured vesicle structure is independently validated by a recent modeling study (which was based on the crystal structures of the constituent proteins and stoichiometric knowledge from biochemical studies). However, we also present, to our knowledge, the first evidence of a laterally anisotropic structure on the vesicle surface, indicative of large protein clusters. Hence, not only has SAXS refined our knowledge of SV structure, it now seems likely it can be used to enable us to more fully understand other biological membranes.

MATERIALS AND METHODS

Purification of synaptic vesicles

Synaptic vesicles were purified from rat brain, as described in Takamori et al. (4), through differential centrifugation, sucrose density centrifugation, and size-exclusion chromatography. Although SVs prepared this way are 95% pure (as measured by immunogold electron microscopy for integral SV membrane proteins), some larger membranous structures remain after purification (100–200 nm). These particles (<0.9% of the total number of particles) have a significant influence on the scattering intensity. Analytical tools were developed to account for this (see later in this article). After chromatography, an additional centrifugation step was introduced to allow buffer exchange and SV concentration. SVs were resuspended in HB100 (in mM; 100 KCl, 1 DTT, 25 HEPES, pH 7.40 KOH), and immediately snap-frozen for transportation to the synchrotron. Importantly, membrane damage due to freeze/thaw was minimal as judged by the capacity of the SVs to acidify (7). The dry weight of the SV population was obtained by measuring the protein mass using a modified Lowry assay and assuming a constant (10:5:2) ratio of proteins, phospholipids, and cholesterol (4). The resulting SV stock solutions had a protein concentration in the range of 6 μg/μL. No aggregation was observable either by electron microscopy (EM) or dynamic light scattering (not shown).

Cryo-electron microscopy

To provide an independent measure of the relative size polydispersity $p_n(R)$ of the SV population, cryo-electron microscopy (cryo-EM) measurements were performed on vitrified SV solutions, using a Titan Krios microscope (Cs-corrected; FEI, Hillsboro, OR) operating at 300 kV, and equipped with an Eagle 4K (FEI) charge-coupled device (CCD), running in twofold binning mode. Samples were first bound in a Vitrobot Mark IV (FEI) to a glow-discharged "holey" carbon foil (quantifoil grid). Samples were then blotted twice for one second at "blot-force" 2 and subsequently vitrified at 30°C and 97% humidity. In total, 559 SVs were measured and R was determined by taking the average of the shortest and longest diameter of the SVs, as measured from bilayer surface to bilayer surface.

To characterize the larger membranous particles, EM tilt-pair images at 0 and 45° relative angles were taken with a model No. CM200 FEG microscope (Philips Medical, Foster City, CA) and recorded using a 4K×4K slow-scan CCD (TVIPS, Oslo, Norway), running in twofold binning mode (FEI). These were used to assess the sampling error caused by uneven collapse of particles onto the carbon grid.

Small-angle x-ray scattering

SAXS experiments were performed at the high brilliance undulator beam line ID-2 at the European Synchrotron Radiation Facility in Grenoble, France, operating under the beam line's standard conditions of 12.4 keV photon energy (8). The SV samples were at a total protein concentration of 2.74 μg/μL in aqueous buffer (HB100). The samples were kept in a glass flow-through capillary with a diameter of 1.5 mm and a wall thickness of 0.01 mm. The diffraction patterns were recorded with a FReLoN CCD detector (ESRF, Grenoble, France) positioned 0.85 and 5 m behind the sample in an evacuated detector tube. Data was collected over a q-range from 0.016 to 5.5 nm^{-1}. A typical exposure time was 0.1 s. The two-dimensional isotropic (powder average) diffraction pattern was corrected for the CCD dark current, offset of the analog to digital converter, spatial distortion, and detector sensitivity (flat-field), and was calibrated to the absolute scale (water reference) employing a previously described procedure (9). Data recorded at the two different detector distances was combined to give a corrected scattering curve $I(q)$, covering more than two orders of magnitude in q. Radiation damage was ruled out by comparison of scattering patterns recorded with different exposure times from 0.01 to 10 s. For the standard accumulation time, the absorbed dose during exposure was ~6.5×10^3 Gy. Dilution series revealed no measurable interparticle correlations or aggregation for samples with total protein concentrations between 6.45 and 1.29 μg/μL.

Scattering form factor model

The scattering cross section for a dilute, polydisperse system of particles of radius R with the number size distribution $p(R)$, the volumes $V(R)$, and the scattering form factor $P(q, R)$ is given by (10)

$$\frac{d\sigma(q)}{d\Omega} = \Delta\rho^2 \int_0^\infty p(R)V(R)^2P(q,R)\, dR, \qquad (1)$$

where $V(R)$ is the dry volume of the particle defined as the total volume V_{tot} minus the volume of the solvent core V_{core}. The value $p(R)$ was used as determined by cryo-EM (smoothed), together with an additional freely varied Gaussian contribution to account for the trace number of larger membranous particles in the sample. The expression $\Delta\rho = M/V$ denotes the difference between the scattering length density of the solvent and the average scattering length density of the decorated bilayer. The notation M will be used below as the total excess scattering length of a particle. The total number of electrons within the particle population is

$$N_e = (\rho_0 + \Delta\rho_e)\int_0^\infty p(R)V(R)\, dR,$$

with ρ_0 denoting the electron density of the solvent, and $\Delta\rho_e$ the average excess electron density of the decorated bilayer. The dry mass m of the particle population can be obtained from the Lowry assay, and can be directly linked to N_e, assuming a fixed ratio of 1.87 neutrons or protons per electron within the particles (11,12) and considering the electron density of the buffer (333 electrons/nm^3). Thus, $\Delta\rho$ and the number size distribution $p(R)$ can both be obtained on an absolute scale. As always in scattering experiments, two solutions generally exist for $\Delta\rho$ (and thus $p(R)$) due to Babinet's principle. Here we choose $\Delta\rho > 0$, in agreement with the existing data on bilayer densities.

The form factor model is built from a central bilayer profile (13–15) with added protein shells on the inside (lumen) and outside of the SV. The spherically symmetric electron density profile of the bilayer is modeled by three concentric Gaussians (16), representing the headgroups of the two lipid leaflets and the hydrophobic core (see *light shaded areas* in Fig. 3 *C*). Note that protein residues associated with the headgroups and *trans*-membrane protein segments are included in this contribution. The larger proteins, or protein clusters, of the inner and outer protein shells, which can be clearly seen in the cryo-EM images seen later in Fig. 2, *B* and *C*, are modeled by Gaussian chains (17) attached to the inner and outer sides of the bilayer, respectively (18) (*dashed lines* and *dark shaded areas* seen later in Fig. 3 *C*). A sketch of the corresponding model in real space is given in Fig. 1 *B*. This approach is a generalization of a model originally derived for polymer-modified micelles and liposomes ((18), L. Arleth and C. Vermehren, unpublished). For comparison, Fig. 1 *A* shows a section through a molecular model of an average SV,

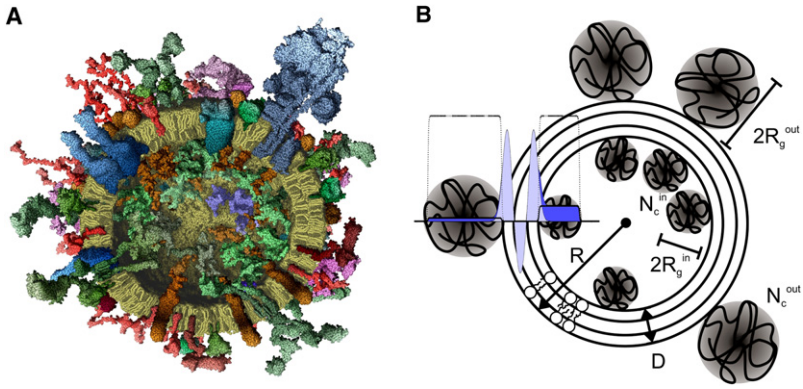

FIGURE 1 (*A*) Section through a molecular model of an average SV isolated from rat brain, based on space-filling models of macromolecules at near-atomic resolution. Reproduction from Takamori et al. (4). (*B*) Sketch of a real-space model corresponding to an optimized scattering form factor consistent with the measured SAXS data. (For details on the model and parameters, see Tables 1 and 2, Fig. 3, and the Appendix.)

based on space-filling models of macromolecules at near-atomic resolution (reproduction from (4)). The contribution of the Gaussian chains explicitly introduces an in-plane structure to the model, breaking the spherical symmetry. The individual Gaussian chains are assumed to be perfectly uncorrelated, forming an ideal gas on the sphere. The extension of the Gaussian chains in the radial direction might be interpreted as the thickness of the protein layers, whereas the lateral extension (parallel to the membrane tangent plane) may reflect the in-plane size of individual proteins, protein clusters, and/or distinct lipid microdomains in a coarse-grained sense. For the calculation of polydisperse populations, the local structure of the bilayer profile and the Gaussian chain layers including the density of Gaussian chains within the chain layers were kept constant for all population members. Least-squares fitting was performed using the *lsqnonlin* routine of MATLAB Optimization Toolbox (Ver. 7.5.0.342 (R2007b); The MathWorks, Natick, MA), dedicated to solve nonlinear least-squares problems. Statistical error analysis within the linear approximation was performed using the *nlparci* routine of MATLAB Statistics Toolbox (The MathWorks), based on an asymptotic normal distribution of the residuals. One main source of systematic errors is the uncertainty in the absolute scale of the data.

The model parameters given in Table 1 were subject to optimization during the fitting procedure of the form factor model to $I(q)$ and include a small constant background and three parameters reflecting the freely varied Gaussian component of $p(R)$, accounting for larger membranous particles in the sample. The part of $p(R)$ representing the size distribution of the SVs as obtained by cryo-EM was kept constant. For both branches of $p(R)$, the same form factor was used. In particular the bilayer profile parameters and the density of Gaussian chains per surface area

$$N_c^{in}/\left(4\pi\left(R-D-R_g^{in}\right)^2\right) \text{ and } N_c^{out}/\left(4\pi\left(R+R_g^{out}\right)^2\right)$$

were kept constant. The effective number of free parameters was 12. However, it should be emphasized that the 12 parameters were, in practice, only free to vary within relatively narrow intervals due to the structural constraints to these parameters imposed by the model. (See Appendix for further details on the scattering form factor.)

RESULTS

Cryo-EM

Fig. 2 *A* shows the size distribution of SVs as determined by the analysis of cryo-EM images of 559 SVs. The SV radius R was determined from the diameter of the SV, measured from bilayer surface to bilayer surface. The most frequently occurring size is $R = 21$ nm. The size distribution runs from $R = 15$ to $R = 30$ nm, and drops off asymmetrically with a slower descent toward larger radii than toward smaller. Fig. 2, *B* and *C*, shows typical cryo-EM micrographs of SVs. Clearly visible are proteins extending both to the outside and the lumen of the SV, and the characteristic lipid bilayer structure.

SAXS

Fig. 3 *A* shows the SAXS intensity function $I(q)$ for a typical SV sample (*black circles*) and a least-squares fit (reduced $\chi^2 = 2.84$) to the form factor model (*solid red line*) for

TABLE 1 Parameter values with 95% confidence bounds as obtained, from the optimized anisotropic SAXS models

Model fit parameter	Gaussian chain coronas	Hard sphere coronas*	(Unit)
$\rho_{in} + 333$, $\rho_{out} + 333$	379.8 ± 1.3	375.7 ± 0.5	(e^-nm^{-3})
$\rho_{tail} + 333$	304.2 ± 3.2	99.9 ± 46.1	(e^-nm^{-3})
$t_{in}\sqrt{2\pi}$, $t_{out}\sqrt{2\pi}$	1.8 ± 0.2	2.9 ± 0.2	(nm)
$t_{tail}\sqrt{2\pi}$	2.1 ± 0.2	0.6 ± 0.2	(nm)
R_g^{in}	3.2 ± 0.1	2.4 ± < 0.1	(nm)
R_g^{out}	5.7 ± 0.3	5.6 ± 0.1	(nm)
$N_c^{in}/(4\pi(R - D - R_g^{in})^2)$	(7.09 ± 0.99) × 10^{-3}	(13.75 ± 0.95) × 10^{-3}	(nm^{-2})
$N_c^{out}/(4\pi(R + R_g^{out})^2)$	(0.47 ± 0.05) × 10^{-3}	(0.42 ± 0.03) × 10^{-3}	(nm^{-2})
$\rho_c + 333$	385.1 ± 1.5	399.0 ± 1.4	(e^-nm^{-3})
Mean radius larger particles	210.1 ± 7.2	232.5 ± 21.1	(nm)
Width distribution larger particles	50.2 ± 2.8	54.5 ± < 0.1	(nm)
Number larger particles	(0.56 ± 0.04) × 10^9	(0.42 ± 0.06) × 10^9	(μL^{-1})
Constant background	(−14.8 ± 2.9) × 10^{-6}	(13.5 ± 22.6) × 10^{-6}	(mm^{-1})

*$R_g^{in} = R^{in}$ and $R_g^{out} = R^{out}$.

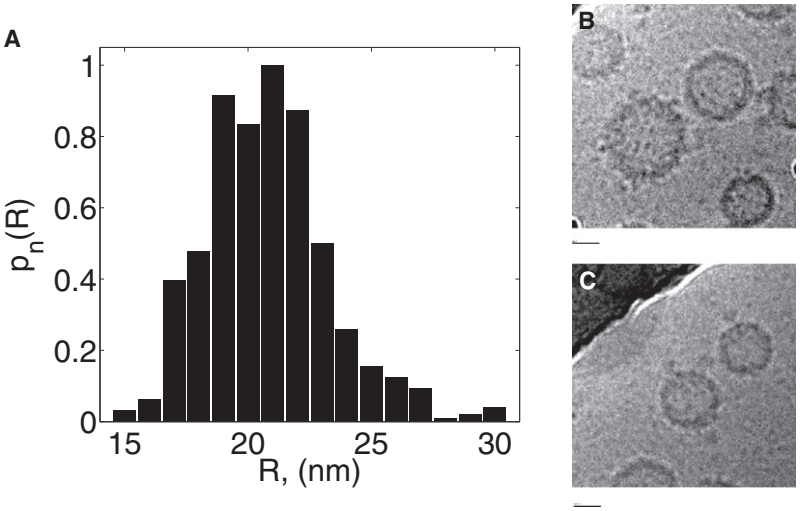

FIGURE 2 (*A*) EM size distribution of SVs from rat brain. (*B* and *C*) Cryo-EM images of typical SVs from rat brain. Scale bars, 20 nm.

bilayer vesicles with Gaussian random coils attached to the inside and outside, as detailed in the Appendix. Fig. 3 *B* shows the corresponding bimodal size polydispersity distribution function $p(R)$ of the SVs. Again a bimodal distribution function $p(R)$ was used, with the left branch corresponding to the cryo-EM data and the right branch corresponding to the larger membranous particles, modeled by a Gaussian distribution centered at ~210 nm with a standard deviation of 50 nm. It should be emphasized that due to the resolution of the SAXS technique, our data are relatively insensitive to the exact size distribution of these larger particles. Fig. 3 *C* shows the radial electron density distribution $\rho_e(r)$ for an SV with the most frequently occurring radius (bilayer surface at $r \simeq 21$ nm), corresponding to the fit (*solid line*) in Fig. 3 *A*.

Fig. 4 shows the SAXS intensity function $I(q) \times q^2$ versus q for a typical SV sample (*black circles*) and a least-squares fit to the form factor model (*solid red line*). The SAXS curve exhibits a characteristic pattern, well distinct from that of

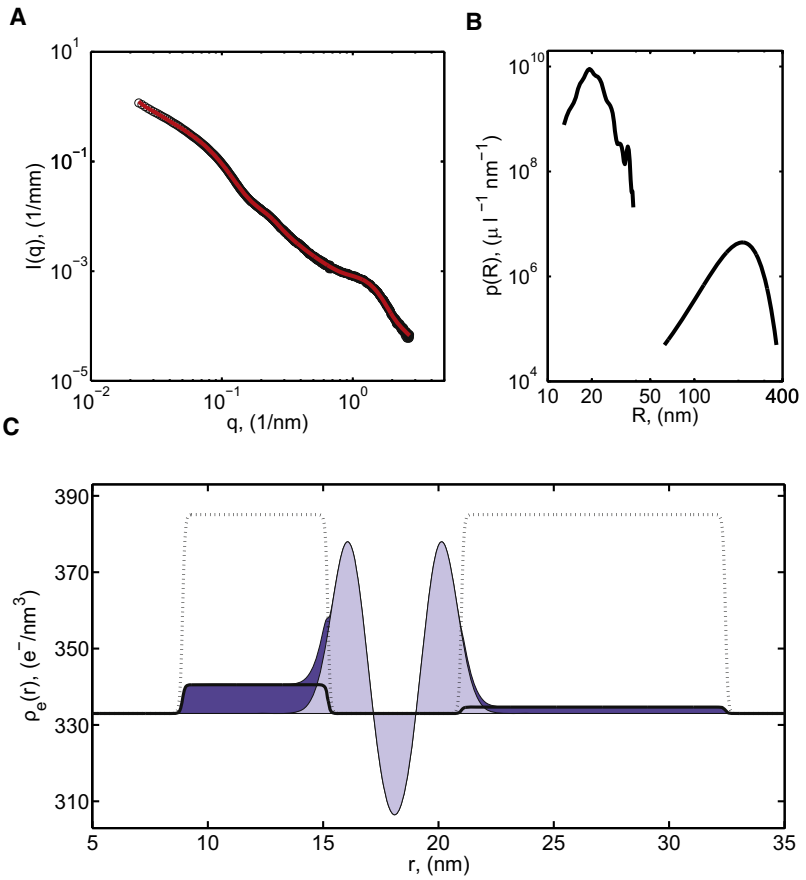

FIGURE 3 (*A*) SAXS data (*black circles*) and least-square fit (*solid red line*). (*B*) Bimodal size distribution function $p(R)$ employed in the form factor calculation. Binning size, 1 nm. (*C*) Calculated electron density distribution $\rho_e(r)$ across a SV membrane. (*Dotted line*) Typical maximum local contribution of Gaussian chains. (*Solid line*) Spherically averaged contribution of Gaussian chains. (*Light shaded area*) Lipid bilayer. (*Darker shaded area*) Spherically averaged contribution of protein layer.

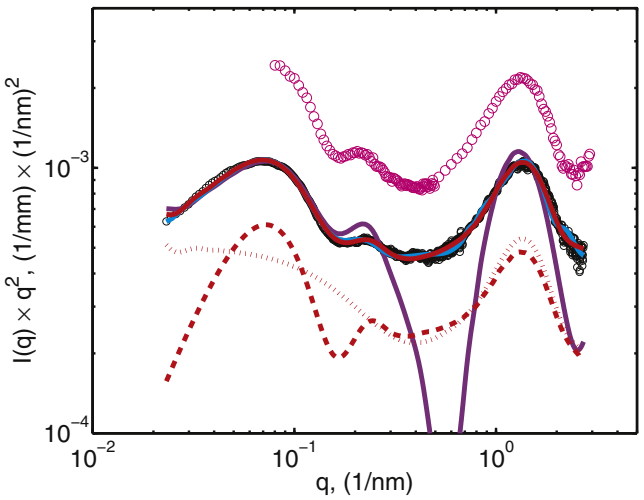

FIGURE 4 SAXS data of different SV preparations taken at ID-2/ESRF (*black circles*, as in Fig. 3 *A*) and HASYLAB, beam line B1 (*magenta circles*, shifted for clarity). Least-squares fit of a spherical symmetric model (*solid purple line*) assembled from five coupled Gaussian-shaped electron densities. Least-squares fit (*solid blue line*) of a model assembled from three coupled Gaussian-shaped electron densities with hard-sphere coronas on the inside and outside. Least-squares fit (*solid red line*) of a model assembled from three coupled Gaussian-shaped electron densities with Gaussian chain coronas on the inside and outside. Contributions to the calculated scattering originating from the SV population (*left branch* of $p(R)$; *dashed red line*) and from the larger particles (*right branch* of $p(R)$; *dotted red line*).

pure lipid vesicles. These data are the same as in Fig. 3 *A*. The contributions to this least-squares fit (*solid red line*) arising from the two branches of the bimodal size polydispersity distribution function $p(R)$ are given separately (SVs, *dashed red line*; larger particles, *dotted red line*). In addition, an independent SAXS data set (*magenta circles*), measured using a different SV sample at HASYLAB beam line B1 (DESY, Hamburg, Germany), at 9 keV photon energy, is given for comparison, indicating the reproducibility of the characteristic features of the SV SAXS curve. Note that many batches of SV preparations have been measured and form a very reproducible and consistent set of data. Two least-squares fits (*solid purple line* and *solid blue line*) to different form factor models are described in detail below.

The dry mass of the average SV is 32.5×10^{-18} g, which compares well to values determined by scanning transmission electron microscopy ($(26.9 \pm 6.8) \times 10^{-18}$ g) (4). The total particle concentration in the sample is calculated to be 6.5×10^{10} particles per μL partitioned into 99.1% SVs and ~0.9% larger particles. The theoretical buoyant density of a SV with a radius $R = 21$ nm is ~1.05 g/mL. The characteristic thickness of the concentric Gaussian shells is 5.7 nm, and can be interpreted as an effective thickness of the bilayer structure of the SV. The extension of the Gaussian chains is 6.3 nm (facing inward) and 11.4 nm (facing outward). An SV of size $R = 21$ nm is decorated with an average of 12.9 Gaussian chains on the inside and 4.2 Gaussian chains on the outside. Projected onto the middle of the bilayer structure, these cover ~10% and 11% of the surface area, respectively.

TABLE 2 Best-fit SV model structure with Gaussian chain coronas, $R = 21$ nm

Model property	Numerical value	(Unit)
Dry mass of entire SV	32.5×10^{-18}	(g)
Dry mass of lipid bilayer	26.4×10^{-18}	(g)
Dry mass of Gaussian chains inside	2.0×10^{-18}	(g)
Dry mass of Gaussian chains outside	4.0×10^{-18}	(g)
Number of Gaussian chains inside (N_c^{in})	12.9	(1)
Number of Gaussian chains outside (N_c^{out})	4.2	(1)
Cross section of Gaussian chain inside ($R_g^{in2}\pi$)	31	(nm^2)
Cross section of Gaussian chain outside ($R_g^{out2}\pi$)	103	(nm^2)
Surface coverage of Gaussian chains inside*	10	(%)
Surface coverage of Gaussian chains outside*	11	(%)
Buoyant density of entire SV	1.05	(g/mL)

*Projected onto $r = R_{tail}$.

The structural parameters of the model representing the average SV structure are given in Tables 1 and 2, and confirm the values published in literature and which were derived using biochemical methods (4).

Two other models were also tested during the analysis:

1. A model consisting solely of five concentric Gaussians, i.e., a generalization of Eq. 4, with a symmetric bilayer profile, and one additional Gaussian shell both on the inside and outside, respectively. This model has 11 free parameters.
2. A model consisting of three concentric Gaussians where spherical particles were placed on the inside and outside instead of the Gaussian chains. The later model is similar to that given in Eq. 3 except that P_c^i (Eq. 6) and ψ^i in Eq. 7 are replaced by the scattering form factors of spheres and the scattering form factor amplitudes of spheres, respectively. The spheres are of radii R^{in} and R^{out}, and the number of free model parameters is 12.

A least-squares fit to the SAXS data of the spherical symmetric model (Fig. 4, *solid purple line*) cannot describe the data (reduced $\chi^2 = 601.6$). A further model variant, with an asymmetric bilayer profile, also failed to explain the data (data not shown).

The model with spheres attached to the bilayer profile (Fig. 4, *solid blue line*) yields a least-squares fit to the SAXS data with a reduced $\chi^2 = 4.18$. The structural parameters of the optimized model are given in Table 1. The main features of the model with attached Gaussian chains are replicated in the model with attached spheres. In particular, the parameters of the Gaussian chains and the spheres in the two models indicate that breaking of spherical symmetry is an essential ingredient needed to describe the data well.

Importantly, a least-squares model fit to small lipid (1,2-dioleoyl-*sn*-glycero-3-phosphatidylserine) vesicle data yields almost identical results for a spherically symmetric model with a symmetric density profile consisting of three

coupled Gaussians and a model with Gaussian chains attached to the profile (data not shown). Interestingly, the number of Gaussian chains in the later model is zero for the best fit (within the numerical precision).

None of the fitted curves show distinct features outside the measurement interval, either at small or at high q. In particular, the heterogeneous nature and broad size distribution of the larger particles suppress any pronounced features at lower q-regions.

DISCUSSION

We addressed the size distribution function (polydispersity) $p(R)$, by measuring consistent values with two independent techniques. The SAXS results were obtained on large ensembles and so were subject to intrinsic averaging. In contrast, with cryo-EM, pictures of over 500 individual vesicles were taken to increase statistical relevance. Owing to the strong size-dependent variation of the scattering intensity, SAXS is sensitive to larger particles, which can be minimized, but which are unavoidable during sample preparation.

The resulting size-distribution function $p(R)$ can thus be considered as free of artifacts related to a specific technique, and presumably represents the SV structure averaged across many nerve terminals and with vesicles at all points of the cycling pathway. Some of the structural heterogeneity seen at the cryo-EM level (Fig. 2, *B* and *C*) is likely to be due to heterogeneous occupancy of the vesicle surface by accessory proteins. However, such an average is still likely to be highly informative, because each vesicle contains one isoform of each of the major SV proteins responsible for vesicle function—including synaptobrevin, synaptotagmin, and synaptophysin (4).

In light of the fact that proteins, and protein macromolecular complexes, generally display consistent sizes, the size polydispersity of synaptic vesicles (in agreement with previous electron microscopic studies of intact presynaptic terminals (20)), is surprising to us. Neurotransmitter content is lost during purification (21), so this effect is not caused by increasing osmotic pressure with elevated neurotransmitter concentration inflating vesicles, which is consistent with the observation that membrane bilayers cannot be stretched by >3% (20). A more likely source of size variation comes from the reformation of SVs after exocytosis, via clathrin-mediated endocytosis. Vesicle size is presumably influenced by the size of the clathrin cage initially formed on the plasma membrane—a process controlled by the protein AP180. Clathrin cage formation may be a simple stochastic process, with size determined by recruitment of sufficient AP180, as *Drosophila* neurons lacking AP180 have fewer SVs, which are larger in size (22). Alternatively, clathrin-coat formation may be an active process where the retrieval of sufficient cargo is proof-read (23) and vesicle size can be influenced by the diffusion of synaptic proteins through the membrane following fusion (see below).

What remains unclear is the effect on vesicle function (if any) produced by this polydispersity; vesicles with $R =$ 16 nm and $R = 24$ nm (Fig. 2 *A*) differ by more than a factor-of-two in surface area and a factor-of-three in volume. Among other things, such differences in surface area and volume may have important consequences for the spatial (and functional) arrangement of *trans*-membrane domain proteins in the vesicle and for neurotransmitter content. It remains unclear whether the number of SV proteins scales with vesicle size. However, it is unlikely that vesicles retain a constant number of proteins during their lifetime. Recent studies suggest an exchange of proteins with the plasma membrane during exocytosis (24). We favor a model in which SV composition is effectively variable, with slight infidelities in the recycling process (which are likely to occur under conditions of intense activity) being tolerated. In this respect, the large numbers of essential trafficking proteins on an average SV are understandable, as it allows for a comfortable safety margin during cycling. It needs to be remembered, however, that the concentration of neurotransmitter in the vesicle appears to be determined, to some extent, by the copy number of transporters. This might be one source of variation in the postsynaptic response to single vesicle release events—so-called ''mini'' events. The source of unitary fluctuations may also relate to vesicular volume—although the situation is not entirely clear and may depend on neurotransmitter type. For instance, a clear dependence on vesicle size was found for serotonin content, although no such dependence was found for glutamate (25).

After quantification of polydispersity on an absolute scale, mass on an absolute scale, $m(R)$, can be attributed to a vesicle of a given size. This calculation is based on the calibrated SAXS intensities, as well as the proportionality between scattering length density and mass density (based on a fixed stoichiometry of protons on the scale of the resolution of the experiment). Accordingly, the dry mass of an SV of radius $R = 21$ nm is 32.5×10^{-18} g and its theoretical buoyant density is 1.05 mg/mL—lower than the value of 1.10 g/mL determined experimentally by equilibrium density-gradient centrifugation (4). At present, we are unable to reconcile these two values.

The SAXS data presented here is, by itself, limited due to the low spatial resolution attainable with this technique. The greatest strength of our study relates to the application of independently obtained biochemical data in order to develop a coarse-grained description of the different SV constituents in relation to one another (4). To this end, we address the electron density profile $\rho_e(r)$ from the SAXS analysis, establishing how to interpret the Gaussian chain layers of the model. As SAXS is unable to reach molecular resolution, the Gaussian chains must be considered as effective scattering centers distributed on the lipid bilayer, which can be considered to represent very large proteins or protein clusters of known mass (4). The model parameters can be interpreted beyond the total protein mass, when viewed in

terms of the known protein inventory provided by biochemical analysis (4), whereas the (effective) length-scale indicated by the radii of gyration R_g of the Gaussian chains can also be postulated. According to Takamori et al. (4) (expressed below as weight % of total SV proteins, copy-number per SV, and number of *trans*-membrane domains per molecule), the major protein components of an average vesicle isolated from rat brain are:

Synaptophysin 1 (10.2, 31.5, 4)
Synaptobrevin 2 (8.6, 69.8, 1)
VGLUT, averaged for VGLUT1- and VGLUT2-containing vesicles (6.0, 10.0, 10)
Synapsin 1 (6.0, 8.3, 0)
Synaptotagmin 1 (7.0, 15.2, 1)
Rab3A (2.5, 10.3, 0)
Syntaxin 1 (2.0, 6.2, 1).

These proteins (which are essential for both exocytosis and neurotransmitter loading) account for ~50% of the total SV protein inventory, corresponding to 151 individual protein molecules, with a total of 319 *trans*-membrane domains. However, as only the dominant isoform was measured for most proteins including synaptophysin, synaptobrevin, and synaptotagmin, the copy-number of each protein is likely to be higher. When taking into account other proteins, such as the V-ATPase complex and synaptogyrin, it is likely that the integral membrane proteins contribute almost 600 *trans*-membrane domains (4). For an average $R = 21$ nm vesicle, this would equate to ~20% of the surface (4), in excellent agreement with the 21% surface coverage of the Gaussian chains.

The V-ATPase is the largest protein on the vesicle and faces outward. Although it is only present in one or two copies, its large size means it contributes 1.2% of the total protein mass. In our model, the Gaussian chains facing outward contribute ~12.4% of the total mass of a vesicle (see Table 2), and thus ~21.1% of the total protein mass (4). At most, 5.7% of the mass represented by the outward facing Gaussian chains can be attributed to the V-ATPase. The remaining 94.3% of the protein mass in the Gaussian chains cannot be attributed to individual protein components. First, the individual copy-numbers would be too low. Second, the lateral extension would be too large. Although extended proteins such as synaptobrevin could account for a $2R_g^{out} = 11.4$-nm extension in the radial direction (26), the corresponding lateral size indicates a clustering of proteins into domain structures, as there are too few (known) large proteins on the vesicle that match the size of the Gaussian chains in the in-plane direction. Interestingly, cholesterol-dependent clustering of the synaptic vesicle proteins synaptobrevin, synaptotagmin, and synaptophysin into domains has been reported in a crude synaptic vesicle preparation (27), suggesting that the fusion apparatus might be concentrated in a specialized membrane patch. This clustering might have important consequences for vesicle function. For instance, the vesicular SNARE protein synaptobrevin, which interacts with syntaxin 1 and SNAP-25 in the plasma membrane to initiate fusion, has a cytosolic length of ~10 nm, as do syntaxin and SNAP-25. Given that SNARE interactions are initiated N-terminally and proceed toward the C-terminus in a zipperlike fashion, thus pulling the membranes together, it is likely that SNARE initiation can proceed from a distance of up to 20 nm from the plasma membrane, a value consistent with that proposed by single-vesicle tracking experiments in living neurons (26).

SUMMARY

In summary, the scattering model used here is in excellent agreement with the SAXS data, using parameters that are consistent with published electron microscopic, biochemical, and physiological data. At the same time the resulting model was obtained independently of other analytical techniques. This study thus confirms preexisting ideas about the main structural features of SVs, and adds important refinements, such as the presence of protein microdomains. To the best of our knowledge, this is the first time SAXS has been successfully applied to a functional (heterogeneous) organelle and raises the distinct possibility that SAXS analysis (when applied in combination with other analytical approaches) will provide a useful means to analyze other biological membranes.

APPENDIX: SCATTERING FORM FACTOR

Equation 3 (below) gives the final form factor used in the fitting procedure. The model is built from a central bilayer profile with added protein shells on the inside (lumen) and outside of the SV. Although we give the resulting equation and sketch the derivation here, our intention is to describe the model more fully in a forthcoming publication. The bilayer electron density profile is modeled by three concentric Gaussians (16), representing the headgroups of the two lipid leaflets and the hydrophobic core. Note amino acid residues associated with the headgroups and *trans*-membrane protein segments are included in this contribution. The inner and outer protein shells are modeled by Gaussian chains (17) attached to the inner and outer sides of the bilayer, respectively ((18,28,29), L. Arleth and C. Vermehren, unpublished). A sketch of the corresponding model in real-space is given in Fig. 1 *B*. The excess scattering length density of the bilayer profile is given by

$$\rho(r) = \sum_{i=1}^{3} \rho_i \exp\left(-(r - R_i)^2/\left(2t_i^2\right)\right), \qquad (2)$$

with the peak position R_i, amplitude ρ_i, and width t_i with $i \in$ in, out, tail, for each of the three Gaussians representing the headgroups of the two leaflets and the tail region, respectively. The (characteristic) radius R is defined as

$$R = R_{out} + t_{out}\sqrt{2\pi}/2,$$

mimicking an SV with the outer lipid bilayer surface at $r \simeq R$. To reduce the number of model parameters, we choose

$$R_{tail} = R - (t_{out} + t_{tail}/2)\sqrt{2\pi},$$

$$R_{\mathrm{in}} = R - (t_{\mathrm{out}} + t_{\mathrm{tail}} + t_{\mathrm{in}}/2)\sqrt{2\pi},$$

and

$$t_{\mathrm{in}} = t_{\mathrm{out}}\ (\text{symmetric bilayer}).$$

Thus, the thickness of the bilayer is characterized by

$$D = \sqrt{2\pi}(t_{\mathrm{in}} + t_{\mathrm{tail}} + t_{\mathrm{out}}).$$

The total excess scattering length with respect to the aqueous buffer is β_{b}. There are $N_{\mathrm{c}}^{\mathrm{in}}$ and $N_{\mathrm{c}}^{\mathrm{out}}$ Gaussian chains distributed randomly and without correlations forming the inner and outer protein shell, respectively. The individual Gaussian chains are characterized by their root mean-square radius of gyration, $R_{\mathrm{g}}^{\mathrm{in}}$ and $R_{\mathrm{g}}^{\mathrm{out}}$, and their common average excess scattering length density ρ_{c}. The distance between the inner headgroup maximum of the bilayer profile and the center-of-mass of the Gaussian chains facing the lumen is taken to be

$$t_{\mathrm{in}}\sqrt{2\pi}/2 + R_{\mathrm{g}}^{\mathrm{in}},$$

and the distance between the outer headgroup maximum and the center-of-mass of the Gaussian chains facing outward is taken to be

$$t_{\mathrm{out}}\sqrt{2\pi}/2 + R_{\mathrm{g}}^{\mathrm{out}}.$$

This limits the penetration of the Gaussian chains into the bilayer, although there is some remaining overlap, mostly due to the extending tails of the bilayer profile (18). The form factor corresponding to the above model can be calculated in kinematic scattering theory, yielding the result

$$\begin{aligned} P(q,R) = \frac{1}{M^2} \times \Bigg[& \beta_{\mathrm{b}}^2 F_{\mathrm{b}}^2(q,R) + \sum_{i=\mathrm{in,out}} N_{\mathrm{c}}^i \beta_{\mathrm{c}}^{i\,2} P_{\mathrm{c}}^i(q) \\ & + \sum_{i=\mathrm{in,out}} 2N_{\mathrm{c}}^{i\,2} \beta_{\mathrm{b}} \beta_{\mathrm{c}}^i S_{\mathrm{b\,c}}^i(q,R) \\ & + \sum_{i=\mathrm{in,out}} N_{\mathrm{c}}^i \left(N_{\mathrm{c}}^i - 1\right) \beta_{\mathrm{c}}^{i\,2} S_{\mathrm{c}}^i(q,R) \\ & + S_{\mathrm{c}}^{\mathrm{in\ out}}(q,R) \prod_{i=\mathrm{in,out}} N_{\mathrm{c}}^i \beta_{\mathrm{c}}^i \Bigg]. \end{aligned} \tag{3}$$

The symbols and functions are given below. $M = \beta_{\mathrm{b}} + N_{\mathrm{c}}^{\mathrm{in}} \beta_{\mathrm{c}}^{\mathrm{in}} + N_{\mathrm{c}}^{\mathrm{out}} \beta_{\mathrm{c}}^{\mathrm{out}}$ denotes the excess scattering length, with $\beta_{\mathrm{c}}^{\,i} = \rho_{\mathrm{c}} R_{\mathrm{g}}^{\,i3} 4\pi/3$ and $i =$ in, out representing the total excess scattering length of a single chain on the outside and on the inside of the bilayer profile, respectively. The normalized amplitude of the self-correlation term of the bilayer profile is given by

$$F_{\mathrm{b}}(q,R) = \sum_{i=\mathrm{in,tail,out}} \frac{F_{\mathrm{b}\,i}(q,R_i)}{M_{\mathrm{b}\,i}} \tag{4}$$

with

$$\begin{aligned} F_{\mathrm{b}\,i}(q,R_i) = 4\sqrt{2} t_i \rho_i \exp\left(-t_i^2 q^2/2\right) q^{-1} \times \big[& t_i^2 q \cos(qR_i) \\ & + R_i \sin(qR_i) \big], \end{aligned} \tag{5}$$

where

$$M_{\mathrm{b}\,i} = \rho_{\mathrm{i}} \frac{4\pi}{3} \left(\left(R_i + t_i\sqrt{2\pi}/2 \right)^3 - \left(R_i - t_i\sqrt{2\pi}/2 \right)^3 \right)$$

denotes the excess scattering mass of one peak of the bilayer profile (16). The self-correlation terms of the Gaussian chains are given by Debye functions

$$P_{\mathrm{c}}^i(q) = \frac{2[\exp(-x^i) - 1 + x^i]}{x^{i\,2}}, \tag{6}$$

with $x^i = q^2 R_{\mathrm{g}}^{\,i\,2}$ and $i =$ in, out for the inner and outer chains, respectively. The interference cross-terms $S_{\mathrm{b\,c}}^{\mathrm{in}}(q,R)$ and $S_{\mathrm{b\,c}}^{\mathrm{out}}(q,R)$ between the bilayer and the Gaussian chains on the inside and outside, are given by

$$S_{\mathrm{b\,c}}^i(q,R) = F_{\mathrm{b}}(q,R) \psi^i(x^i) \frac{\sin\left(q\left[R_{\mathrm{tail}} \mp \left(D/2 + R_{\mathrm{g}}^i \right) \right] \right)}{q\left[R_{\mathrm{tail}} \mp \left(D/2 + R_{\mathrm{g}}^i \right) \right]}, \tag{7}$$

with $i =$ in, out and $\psi^{\,i}(x^i) = [1 - \exp(-x^i)]/x^i$ the effective form-factor amplitude of the Gaussian chains (30). The product of the scattering form-factor amplitudes of the chains belonging to one of the chain layers with the scattering form-factor amplitude of an infinite thin shell is equivalent to a convolution of the corresponding scattering density distributions in real-space (28) and accounts for the fact that the Gaussian shells are located on a spherical shell,

$$S_{\mathrm{c}}^i(q,R) = \left[\psi^i(x^i) \frac{\sin(q[R_{\mathrm{tail}} \mp (D/2 + R_{\mathrm{g}}^i)])}{q[R_{\mathrm{tail}} \mp (D/2 + R_{\mathrm{g}}^i)]} \right]^2, \tag{8}$$

with $i =$ in, out. The interference term between the chains of the inner and outer shells is taken into account by

$$S_{\mathrm{c}}^{\mathrm{in\ out}}(q,R) = \prod_{i=\mathrm{in,out}} \psi^i(x^i) \frac{\sin\left(q\left[R_{\mathrm{tail}} \mp \left(D/2 + R_{\mathrm{g}}^i \right) \right] \right)}{q\left[R_{\mathrm{tail}} \mp \left(D/2 + R_{\mathrm{g}}^i \right) \right]}. \tag{9}$$

The authors thank Maria Druminski for assistance during SV purification and Ulla Vainio for beam time support.

This work was financially supported by the Excellence Cluster Initiative 171/Deutsche Forschungsgemeinschaft (DFG) Research Center 103, Center for Molecular Physiology of the Brain, DFG SFB 803, and the Max Planck Society. European Synchrotron Radiation Source and HASYLAB are acknowledged for beamtime and excellent working conditions.

REFERENCES

1. Südhof, T. C. 2004. The synaptic vesicle cycle. *Annu. Rev. Neurosci.* 27:509–547.
2. Baumert, M., P. R. Maycox, …, R. Jahn. 1989. Synaptobrevin: an integral membrane protein of 18,000 Daltons present in small synaptic vesicles of rat brain. *EMBO J.* 8:379–384.
3. Nagy, A., R. R. Baker, …, V. P. Whittaker. 1976. The preparation and characterization of synaptic vesicles of high purity. *Brain Res.* 109: 285–309.
4. Takamori, S., M. Holt, …, R. Jahn. 2006. Molecular anatomy of a trafficking organelle. *Cell.* 127:831–846.
5. Alber, F., F. Förster, …, A. Sali. 2008. Integrating diverse data for structure determination of macromolecular assemblies. *Annu. Rev. Biochem.* 77:443–477.
6. Sano, Y., H. Inoue, …, S. Isoda. 1997. Structural analysis of A-protein of cucumber green mottle mosaic virus and tobacco mosaic virus by synchrotron small-angle x-ray scattering. *J. Protein Chem.* 16:151–159.
7. Maycox, P. R., T. Deckwerth, …, R. Jahn. 1988. Glutamate uptake by brain synaptic vesicles. Energy dependence of transport and functional reconstitution in proteoliposomes. *J. Biol. Chem.* 263:15423–15428.

8. Narayanan, T., O. Diat, and P. Boesecke. 2001. SAXS and USAXS on the high brilliance beamline at the ESRF. *Nucl. Instrum. Methods Phys. Res. Sect. A.* 467:1005–1009.

9. Boesecke, P. 2007. Reduction of two-dimensional small- and wide-angle x-ray scattering data. *J. Appl. Cryst.* 40:s423–s427.

10. Guinier, A., and G. Fournet. 1955. Small Angle Scattering of X-Rays. Wiley Interscience, New York.

11. Alberts, B., A. Johnson, …, P. Walter. 2008. Molecular Biology of the Cell, 5th Ed. Garland Science, New York.

12. Howells, E., T. Beetz, …, D. Starodub. 2009. An assessment of the resolution limitation due to radiation-damage in x-ray diffraction microscopy. *J. Electron Spectrosc. Relat. Phenom.* 170:4–12.

13. Bouwstra, J. A., G. S. Gooris, …, H. Talsma. 1993. Small angle x-ray scattering: possibilities and limitations in characterization of vesicles. *Chem. Phys. Lipids.* 64:83–98.

14. Pabst, G., M. Rappolt, …, P. Laggner. 2000. Structural information from multilamellar liposomes at full hydration: full *q*-range fitting with high quality x-ray data. *Phys. Rev. E.* 62(3 Pt B):4000–4009.

15. Pabst, G., R. Koschuch, …, P. Laggner. 2003. Structural analysis of weakly ordered membrane stacks. *J. Appl. Cryst.* 36:1378–1388.

16. Gradzielski, M., D. Langevin, …, R. Strey. 1995. Small-angle neutron scattering from diffuse interfaces. *J. Phys. Chem.* 99:13232–13238.

17. Debye, P. 1947. Molecular weights of proteins from light scattering. *J. Phys. Colloid Chem.* 51:18–32.

18. Pedersen, J. S., and M. C. Gerstenberg. 1996. Scattering form factor of block copolymer micelles. *Macromolecules.* 29:1363–1365.

19. Reference deleted in proof.

20. Qu, L., Y. Akbergenova, …, T. Schikorski. 2009. Synapse-to-synapse variation in mean synaptic vesicle size and its relationship with synaptic morphology and function. *J. Comp. Neurol.* 514:343–352.

21. Burger, P. M., E. Mehl, …, R. Jahn. 1989. Synaptic vesicles immunoisolated from rat cerebral cortex contain high levels of glutamate. *Neuron.* 3:715–720.

22. Zhang, B., Y. H. Koh, …, H. J. Bellen. 1998. Synaptic vesicle size and number are regulated by a clathrin adaptor protein required for endocytosis. *Neuron.* 21:1465–1475.

23. Loerke, D., M. Mettlen, …, S. L. Schmid. 2009. Cargo and dynamin regulate clathrin-coated pit maturation. *PLoS Biol.* 7:e57.

24. Fernández-Alfonso, T., R. Kwan, and T. A. Ryan. 2006. Synaptic vesicles interchange their membrane proteins with a large surface reservoir during recycling. *Neuron.* 51:179–186.

25. Edwards, R. H. 2007. The neurotransmitter cycle and quantal size. *Neuron.* 55:835–858.

26. Zenisek, D., J. A. Steyer, and W. Almers. 2009. Transport, capture and exocytosis of single synaptic vesicles at active zones. *Nature.* 406: 849–854.

27. Jia, J. Y., S. Lamer, …, V. Haucke. 2006. Quantitative proteomics analysis of detergent-resistant membranes from chemical synapses: evidence for cholesterol as spatial organizer of synaptic vesicle cycling. *Mol. Cell. Proteomics.* 20:60–71.

28. Pedersen, J. S. 2000. Form factors of block copolymer micelles with spherical, ellipsoidal and cylindrical cores. *J. Appl. Cryst.* 33:637–640.

29. Pedersen, J. S. 2001. Structure factors effects in small-angle scattering from block copolymer micelles and star polymers. *J. Chem. Phys.* 114:2839–2846.

30. Hammouda, B. 1992. Structure factor for starburst dentrimers. *J. Polym. Sci. [B].* 30:1387–1390.